

Liquid metal for high-entropy alloy nanoparticles synthesis

<https://doi.org/10.1038/s41586-023-06082-9>

Received: 24 May 2021

Accepted: 13 April 2023

Published online: 14 June 2023

 Check for updates

Guanghui Cao^{1,10}, Jingjing Liang^{2,10}, Zenglong Guo^{3,10}, Kena Yang^{1,10}, Gang Wang³, Huiliu Wang¹, Xuhao Wan⁴, Zeyuan Li⁵, Yijia Bai⁶, Yile Zhang¹, Junlin Liu¹, Yanpeng Feng⁷, Zhenying Zheng¹, Cai Lu⁸, Guangzhi He¹, Zeyou Xiong¹, Ze Liu⁹, Shengli Chen¹, Yuzheng Guo⁴✉, Mengqi Zeng¹✉, Junhao Lin^{3,9}✉ & Lei Fu^{1,2}✉

High-entropy alloy nanoparticles (HEA-NPs) show great potential as functional materials^{1–3}. However, thus far, the realized high-entropy alloys have been restricted to palettes of similar elements, which greatly hinders the material design, property optimization and mechanistic exploration for different applications^{4,5}. Herein, we discovered that liquid metal endowing negative mixing enthalpy with other elements could provide a stable thermodynamic condition and act as a desirable dynamic mixing reservoir, thus realizing the synthesis of HEA-NPs with a diverse range of metal elements in mild reaction conditions. The involved elements have a wide range of atomic radii (1.24–1.97 Å) and melting points (303–3,683 K). We also realized the precisely fabricated structures of nanoparticles via mixing enthalpy tuning. Moreover, the real-time conversion process (that is, from liquid metal to crystalline HEA-NPs) is captured *in situ*, which confirmed a dynamic fission–fusion behaviour during the alloying process.

High-entropy alloys (HEAs) have gained continuous interest as a desirable functional material in widespread applications^{1–3,5}. When the size of HEAs decreases to the nanoscale, the high specific surface area, strong synergistic effect, tailororable compositional variation and severe lattice distortion make high-entropy alloy nanoparticles (HEA-NPs) a dream platform for numerous surface reactions^{6–9}. The vastly different chemical and physical properties of mixing elements lead to substantial immiscibility during the alloying reaction^{3,10}. Although it has been reported that the high entropy can enhance the tendency of forming a uniform phase¹¹, a high requirement for extreme heating temperature is always essential in the synthesis to provide a high mixing entropy, which further needs to quench the alloying reaction to preserve the high-entropy state^{3,5,12}. The autocatalytic behaviour of noble elements could also be used in HEA-NP synthesis with reduced reaction temperature yet is only realized in limited systems^{13,14}. Thus far, the development of a synthesis strategy with a high tolerance for synthesis conditions and a wide-range elemental selection is still desirable and challenging.

Considering that the mixing enthalpy of elements represents affinity with each other, the contribution of mixing enthalpy to the HEA formation could not be ignored in addition to mixing entropy^{15,16}. It is promising to obtain HEA-NPs by decreasing mixing enthalpy to reduce Gibbs free energy. In addition to the decreased mixing enthalpy for overcoming the immiscibility issue, the simultaneously dynamic mixing environment in the alloying reaction is also an important promoter. For a dynamic mixing process, the liquid state is usually considered as an

ideal alloying environment in alloy manufacturing strategy. However, reaching the liquid phase needs an extremely high temperature above the melting point of the involved metal elements^{3,16}, which limits the preparation of HEAs. We noticed that certain liquid metal with a low melting point is emerging as a highly desirable candidate in diverse fields^{17–19}. When liquid metal participates in the alloying process, the unique reaction environment may lead to an alloying reaction at low temperature^{20–23}. For example, the room temperature liquid metal Ga, which also possesses negative mixing enthalpy with other metal elements, is an ideal matrix for alloying (Supplementary Table 1)²⁴. Thus, liquid metals could be designed as an ideal reservoir for the preparation of complex multicomponent alloys, which were expected to mix disparate metal elements homogeneously with a high-tolerance condition.

In this study, we realized the synthesis of HEA-NPs with a range of metal elements under mild conditions by using liquid metal reaction media. As illustrated in Fig. 1a, the nanoscale-dispersed liquid metal is utilized as a reservoir to mix with various metal salts as the precursor. Then, the thermal decomposition and hydrogen reduction of the metal salts occur, followed by the metal element mixing in liquid metal, resulting in the formation of HEA-NPs at 923 K. The samples are naturally cooled down to room temperature with a relatively low cooling rate (Supplementary Fig. 1). According to the high-angle annular dark-field scanning transmission electron microscopy (HAADF-STEM) image and the element maps by energy-dispersive X-ray spectroscopy (EDS) (Fig. 1b), the liquid Ga nanoparticle (NP) was uniformly surrounded by the amorphous coating layer consisting of gallium oxide and mixed

¹College of Chemistry and Molecular Sciences, Wuhan University, Wuhan, China. ²The Institute for Advanced Studies, Wuhan University, Wuhan, China. ³Department of Physics and Shenzhen Key Laboratory of Advanced Quantum Functional Materials and Devices, Southern University of Science and Technology, Shenzhen, China. ⁴School of Electrical Engineering and Automation, Wuhan University, Wuhan, China. ⁵School of Power and Mechanical Engineering, Wuhan University, Wuhan, China. ⁶College of Chemical Engineering, Inner Mongolia University of Technology, Hohhot, China. ⁷Bay Area Center for Electron Microscopy, Songshan Lake Materials Laboratory, Dongguan, China. ⁸Department of Engineering Mechanics, School of Civil Engineering, Wuhan University, Wuhan, China. ⁹Quantum Science Center of Guangdong–Hong Kong–Macao Greater Bay Area (Guangdong), Shenzhen, China. ¹⁰These authors contributed equally: Guanghui Cao, Jingjing Liang, Zenglong Guo, Kena Yang. ✉e-mail: ygguo@whu.edu.cn; zengmq_lan@whu.edu.cn; linjh@sustech.edu.cn; leifu@whu.edu.cn

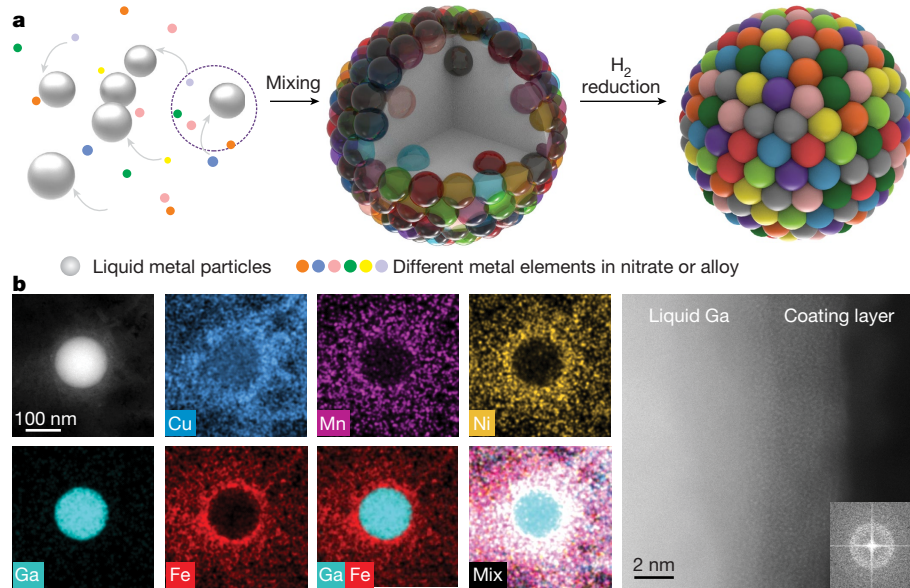


Fig. 1 | Synthesis and characterization of HEA-NPs. **a**, Schematic diagram of the liquid metal-assisted synthesis process. **b**, High-angle annular dark-field EDS elemental maps (left panels) and HAADF-STEM image (right panel) for the

GaFeMnNiCu HEA precursor. The FFT pattern (inset) corresponded to the amorphous coating layer.

metal salts (confirmed by the fast Fourier transform (FFT) pattern) in the precursor. Two adjacent Ga NPs in precursors were also encircled by evenly distributed metal salts (Extended Data Fig. 1). The HEA-NP (GaFeMnNiCu) product is displayed in Extended Data Fig. 2 and Supplementary Fig. 2a. Additionally, the novenary HEA-NPs (GaCaCuPdCo-NiAlMnRu) are also shown in Supplementary Fig. 2b, demonstrating the capability of synthesizing diversified HEA-NPs in a large area. Besides, we have synthesized HEA-NPs with different Ga atomic percentages (Supplementary Fig. 3), demonstrating the tunability of Ga content in the product. The size of HEA-NPs can be tailored by the size of Ga NPs, the reaction temperature and the time (Supplementary Figs. 4–11). The smaller Ga NPs, the lower temperature and the shorter reaction time led to smaller HEA-NPs.

As shown in Fig. 2a, the HEA-NPs with up to 11 dissimilar elements (Cu, Pd, Ni, Mn, Al, In, Ga, Rh, Pt, Co and Mg) are fabricated, where the alloying elements have different preferred crystal structures (face-centred cubic, hexagonal close packed, body-centred cubic and tetragonal). The EDS mapping indicates a uniform distribution of constituent elements in the NP. The atomic-resolution HAADF-STEM image and the FFT pattern demonstrate the high-quality crystallinity of the undecimal HEA-NP. Moreover, the octonary (GaMnNiCuRuRhFeCo), novenary (GaCuPdNiMnInRhPtCo) and 17 (GaFeNiCuZnScVMnMgZrPtRhRuIrHfMoNb) HEA-NPs were also synthesized (Extended Data Fig. 3). We have achieved the preparation of HEA-NPs containing W. Specifically, the quinary GaPdWCuMg HEA-NP contains a wide range of metals with melting points from 303 to 3,683 K. The scanning transmission

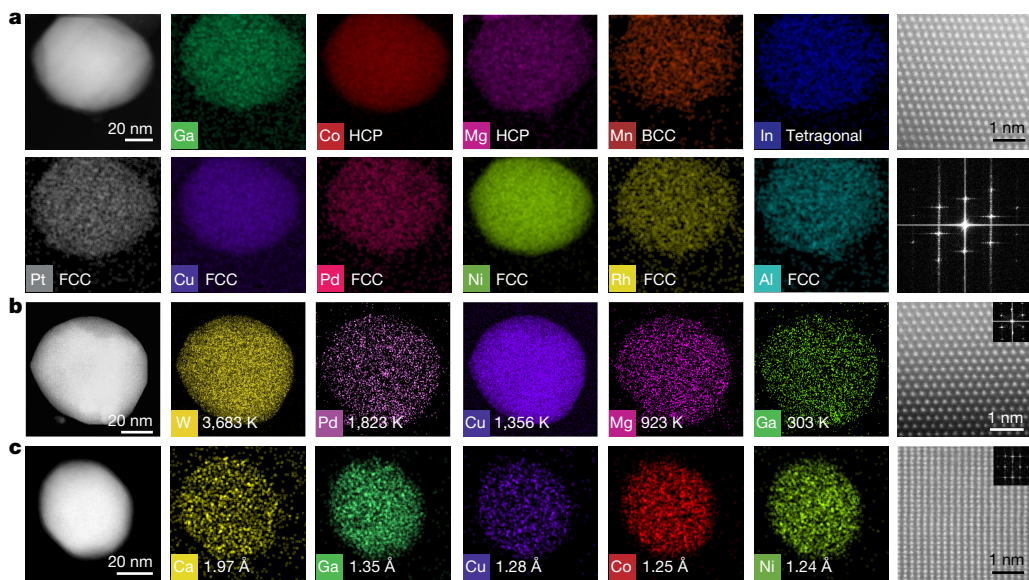


Fig. 2 | Elemental and structural characterization of HEA-NPs. **a**, STEM elemental maps, the HAADF-STEM image and the FFT pattern of an individual undecimal (GaCuPdNiMnAlInRhPtCoMg) HEA-NP, showing the formation of a solid solution structure. **b,c**, STEM elemental maps, the HAADF-STEM

images and the FFT patterns (insets) of GaPdWCuMg (**b**) and GaCuCoCaNi (**c**) HEA-NPs, exhibiting a solid solution structure. BCC, body-centred cubic; FCC, face-centred cubic; HCP, hexagonal close packed.

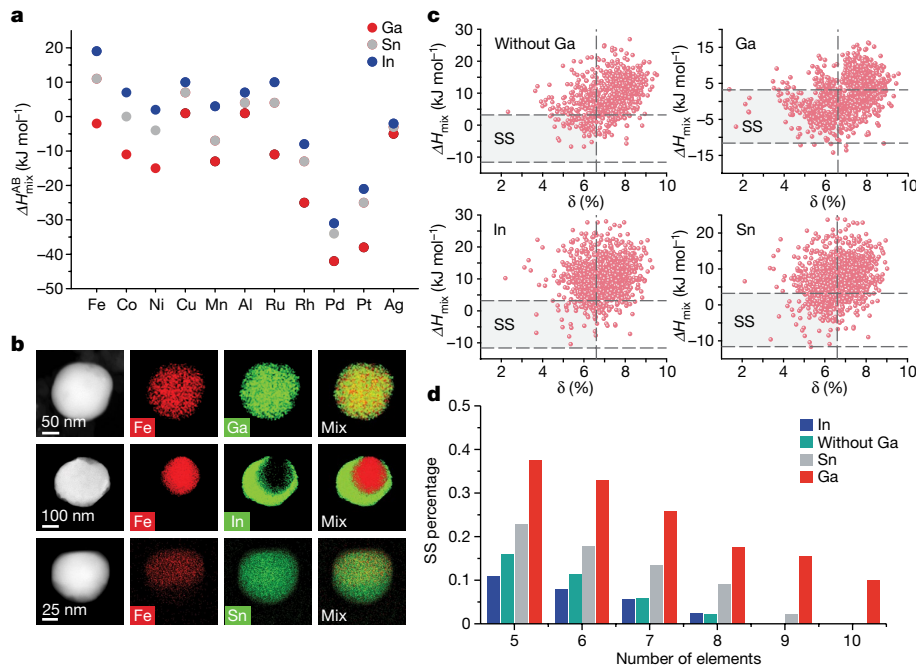


Fig. 3 | The effect of mixing enthalpy on alloy formation. **a**, Statistics diagram of mixing enthalpy among Ga, Sn and In with other elements. **b**, High-angle annular dark-field EDS elemental maps of GaFe/SnFe/InFe systems separately. **c**, The distribution of ΔH_{mix} and δ parameters of HEA

without Ga and containing Ga, In and Sn. **d**, The ratio of the solid solution phase in the compositions shown in **c** as a function of the multi-elemental systems. SS, solid solution.

electron microscopy (STEM) characterizations confirm that the NP is highly crystalline with a uniform elemental distribution (Fig. 2b). Besides, the strategy can also be extended to the HEA-NPs with a sufficiently wide range of atomic radius. Under the Hume–Rothery rule, a binary solid solution can hardly form when the atomic size difference is greater than 15% (ref. 15). Therefore, the formation of HEA-NPs with the large atomic radius difference could demonstrate high elemental inclusiveness of the liquid metal-assisted approach. We realized a wide atomic radius variation from 1.24 to 1.97 Å in quinary GaCuCoCaNi HEA-NPs (Supplementary Fig. 12 and Supplementary Table 2), verified by the STEM characterization in Fig. 2c. Moreover, the HEA-NPs with different particle sizes all exhibited the uniform elemental distribution (Extended Data Fig. 4). Macroscopically, powder X-ray diffraction (XRD) was conducted to further characterize the structure of the products, indicating the formation of a solid solution structure (Supplementary Figs. 13–20). Simultaneously, the powder XRD data of the novenary HEA-NPs in Supplementary Fig. 2b were analysed with Rietveld refinement. The refined results indicate that the sample exhibits a body-centred cubic structure, which matches with the high-angle annular dark-field images along different lattice directions (Supplementary Figs. 21–23 and Supplementary Tables 3–5). The specific alloy compositions are analysed by inductively coupled plasma–atomic emission spectrometry (Supplementary Table 6). Owing to the relatively low vapour pressure of each metal in our mild synthesis condition, the compositional ratio of the product showed a small variation from the starting ratio of the precursor (Supplementary Fig. 24 and Supplementary Table 7).

To investigate the effect of the liquid environment provided by the liquid metal during the formation of HEA-NPs, we performed the synthesis of the alloy without metal Ga. The corresponding system with liquid metal Ga assistance was also prepared, indicating that the liquid environment is beneficial to the realization of HEA-NPs (Supplementary Fig. 25). To understand the origin of overcoming the immiscibility and phase separation, we analyse the thermodynamic parameters in the alloying reaction. According to the Gibbs free energy formula

($\Delta G_{\text{mix}} = \Delta H_{\text{mix}} - T \Delta S_{\text{mix}}$, T is temperature), mixing enthalpy (ΔH_{mix}) is also a critical parameter for alloy formation in addition to mixing entropy (ΔS_{mix}). Binary mixing enthalpy ($\Delta H_{\text{AB}}^{\text{mix}}$) could reflect the interactions between two elements (AB) in the alloy. The $\Delta H_{\text{AB}}^{\text{mix}}$ between liquid metals (Ga, Sn and In) and other elements are presented in Fig. 3a and Supplementary Table 8. The $\Delta H_{\text{AB}}^{\text{mix}}$ of Ga and other elements is lower than that of Sn and In, which indicates a stronger binding force with other elements. We compared two sets of binary alloy systems (GaFe/InFe/SnFe and GaRh/InRh/SnRh) to investigate the effect of the $\Delta H_{\text{AB}}^{\text{mix}}$ on the alloy formation. As shown in Fig. 3b, EDS elemental maps revealed a uniform elemental distribution in GaFe alloy. Nevertheless, apparent element segregation is observed for the In and Sn systems. The elemental distribution is highly related to the $\Delta H_{\text{AB}}^{\text{mix}}$, where the Sn–Fe and In–Fe pairs have more positive $\Delta H_{\text{AB}}^{\text{mix}}$ than Ga–Fe (Supplementary Table 9). GaRh/InRh/SnRh alloys are homogenous due to the good affinity of the elements consistent with the negative $\Delta H_{\text{AB}}^{\text{mix}}$ (Extended Data Fig. 5 and Supplementary Table 9). Therefore, Ga is promising to provide more miscible possibility through its relatively negative mixing enthalpy with other elements.

Based on $\Delta H_{\text{AB}}^{\text{mix}}$, the ΔH_{mix} of HEAs can be calculated from the formulas below¹⁵:

$$\Delta H_{\text{mix}} = \sum_{i=1, i \neq j}^n \Omega_{ij} c_i c_j \quad (1)$$

$$\Omega_{ij} = 4 \Delta H_{\text{AB}}^{\text{mix}} \quad (2)$$

Where Ω_{ij} is an interaction parameter between the i th and j th components, and c_i or c_j is the atomic percentage of the i th or j th component. Combined with the atom radii difference factor (δ), the ΔH_{mix} is considered as the criteria factor to identify the formation of the solid solution phase according to the phase formation rules^{16,25,26}. The solid solution phase can be formed when the value of ΔH_{mix} ranging from -11.6 to 3.2 kJ mol⁻¹ and δ smaller than 6.6% are simultaneously satisfied.

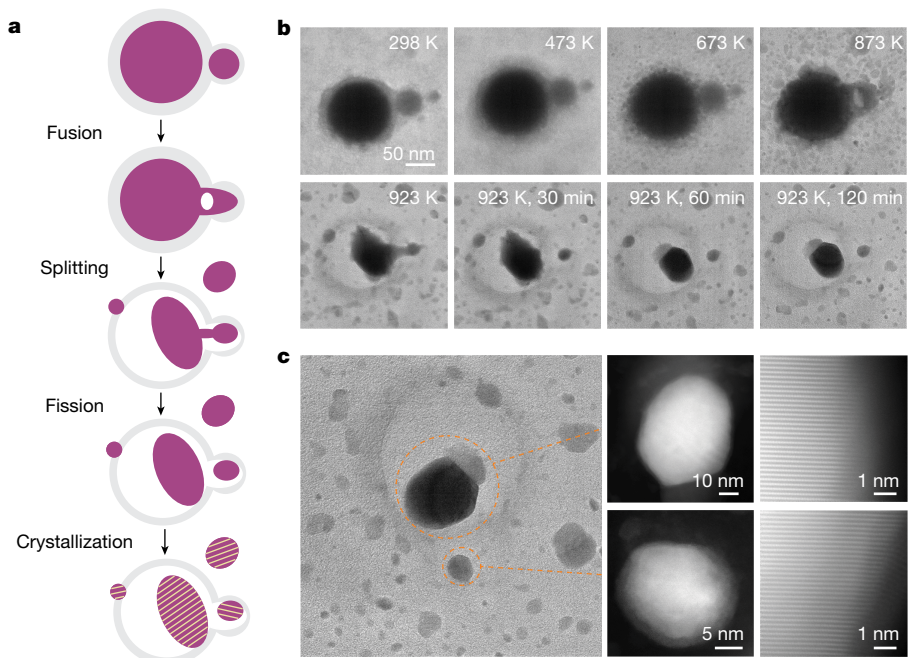


Fig. 4 | The mechanism for the liquid metal-assisted synthesis process.

a, Schematic diagram of the HEA-NPs formation. The transition process from liquid metal NPs wrapped by metal salts to alloy NPs is shown. **b**, In situ transmission electron microscopy visualization of the conversion process from the GaFeMnNiCu precursor to alloy NPs. Sequential images were captured

at 298, 473, 673, 873 and 923 K, and the sample was kept for 30, 60 and 120 min at 923 K. **c**, The corresponding STEM characterization of the GaFeMnNiCu NPs after cooling down to room temperature. The magnified HAADF-STEM images prove that the NPs become crystallized through the in situ experiment.

We explored the phase formation for each equimolar combination of 5, 6, 7, 8, 9 or 10 elements from the palette of these elements (Fe, Co, Ni, Cu, Mn, Mg, Cr, W, Au and Ag) at 923 K. Then, Ga, In and Sn were, respectively, introduced to the above compositions. The phase structures of equimolar combinations from quinary to denary alloys were calculated, where Ga, In and Sn are always included in the corresponding alloy systems. ΔH_{mix} and δ are plotted in Fig. 3c. After introducing Ga, more data points could meet the specific ranges of ΔH_{mix} and δ , which fall into the solid solution phase region. When replacing Ga with In or Sn, the number of compositions satisfying such criteria decreased, which is consistent with the fact that the ΔH_{mix} of both In and Sn are more positive than that of Ga. The ratio of the solid solution phase of the composition space was analysed (Fig. 3d). The systems with Ga have the highest solid solution percentage for the compositions with the same elemental number (that is, the same mixing entropy), demonstrating the ΔH_{mix} has an effect on the formation of the solid solution. The systems from quinary to denary alloys exhibit similar results. Moreover, the quinary alloys (GaFeMnMgCu/InFeMnMgCu/SnFeMnMgCu) were synthesized and characterized (Extended Data Fig. 6), exhibiting the elemental distribution behaviours similar to the GaFe/InFe/SnFe alloys. By decreasing the ΔH_{mix} to reduce the Gibbs free energy, it is also feasible to realize the alloy with uniform elemental distribution in InNiRhPtPd/SnNiRhPtPd alloys. Extended Data Fig. 7 indicated uniform elemental distribution with high-quality crystallinity for the two systems, demonstrating the formation of HEA-NPs.

To investigate the conversion process from the precursor to HEA-NPs, we conducted an in situ experiment to mimic the reaction process in the furnace tube (Fig. 4a). The environmental transmission electron microscopy (ETEM) was utilized to directly observe the dynamical transformation during the reaction process (Fig. 4b). During the heating process with a temperature from room temperature to 923 K, we observed that the Ga NPs flowed and further partially merged (Fig. 4b). The further dynamical fusion process is shown in Supplementary Video 1. Accompanying the fusion of Ga NPs, the surrounding metal elements would coalesce into the Ga NPs. A configuration with two

domains linked by a thin channel formed when the temperature reached 923 K. After keeping the temperature at 923 K for 30 min, the channel splits into two NPs instantaneously (Fig. 4b). Such a fission process can be viewed in Supplementary Video 2 at the interval from 5.32 to 5.46 s. The fusion–fission dynamical process is shown in detail in Supplementary Fig. 26. Moreover, small dispersed NPs appear and disappear frequently in the surrounding area of the liquid precursor during heating, which is additional evidence of the fission behaviour. The fusion–fission behaviour could be attributed to the surface tension variation in liquid Ga NPs and gas release. To accommodate the surface tension change, liquid Ga NPs could deform to release the strain. Besides, the gas, which is produced during the decomposition and reduction of metallic nitrates, could also promote the motion of NPs^{3,12}. As a result, many fusion–fission events of NPs during the alloying process prompt elemental mixing. During the heating process, crystal fringes begin to appear at the partial region of NP (Supplementary Fig. 27). With heating at 923 K for 120 min, the magnified high-resolution transmission electron microscopy (HRTEM) images exhibit crystallization in a large area (Supplementary Fig. 28). After the in situ experiment, the sample was transferred for HAADF-STEM characterizations (Fig. 4c). The lattice fringes of the corresponding two HEA-NPs (Fig. 4b) are further magnified, exhibiting a crystalline state. The element distribution is uniform (Extended Data Fig. 8). This is direct evidence linking the formation mechanism for the formation of HEA-NPs assisted with liquid metal Ga. Furthermore, large-area images were captured (Supplementary Fig. 29), confirming the successful formation of large-scale HEA-NPs.

Moreover, an in situ synchrotron radiation X-ray diffraction (SRXRD) experiment was carried out to further explore the alloy formation process (Supplementary Figs. 30 and 31). The characteristic peaks were observed at the high temperature, demonstrating that the sample underwent crystallization. The peaks were maintained until the cooling process finished, indicating that such a crystalline structure is relatively stable. The cooling process was also simulated by the molecular dynamics based on the machine learning potential, indicating that the crystalline structure can be preserved during cooling (Supplementary Figs. 32

and 33 and Supplementary Table 10)^{27,28}. Therefore, all of the *in situ* ETEM, the *in situ* SRXRD and the dynamic simulation confirmed that the sample crystallized at a high temperature, enabling the sample to tolerate a relatively slow cooling rate without apparent phase separation.

In conclusion, we presented an innovative liquid metal-assisted HEA-NP synthesis strategy with high element inclusiveness under mild conditions. Due to the relatively negative mixing enthalpy between Ga and most metal elements to decrease the Gibbs free energy, the approach by liquid metal Ga assistance can form homogeneous alloys without element separation, which overcomes the immiscibility in alloy systems. We revealed the alloying process from liquid metal to crystalline HEA-NPs via *in situ* ETEM and *in situ* SRXRD characterizations. This alloy strategy can also be expanded to achieve many desirable HEAs oriented by specific applications, where the elemental composition could be designed in a wide range. The in-depth study of the liquid metal reaction mechanism has revealed its dynamic evolution process, which also inspires the methodology based on liquid metals.

Online content

Any methods, additional references, Nature Portfolio reporting summaries, source data, extended data, supplementary information, acknowledgements, peer review information; details of author contributions and competing interests; and statements of data and code availability are available at <https://doi.org/10.1038/s41586-023-06082-9>.

1. Gludovatz, B. et al. A fracture-resistant high-entropy alloy for cryogenic applications. *Science* **345**, 1153–1158 (2014).
2. Li, Z., Pradeep, K. G., Deng, Y., Raabe, D. & Tasan, C. C. Metastable high-entropy dual-phase alloys overcome the strength–ductility trade-off. *Nature* **534**, 227–230 (2016).
3. Yao, Y. et al. Carbothermal shock synthesis of high-entropy-alloy nanoparticles. *Science* **359**, 1489–1494 (2018).
4. Miracle, D. B. High entropy alloys as a bold step forward in alloy development. *Nat. Commun.* **10**, 1805 (2019).
5. Feng, J. et al. Unconventional alloys confined in nanoparticles: building blocks for new matter. *Matter* **3**, 1646–1663 (2020).
6. Xie, P. et al. Highly efficient decomposition of ammonia using high-entropy alloy catalysts. *Nat. Commun.* **10**, 4011 (2019).
7. Li, H. et al. Fast site-to-site electron transfer of high-entropy alloy nanocatalyst driving redox electrocatalysis. *Nat. Commun.* **11**, 5437 (2020).
8. Sun, Y. & Dai, S. High-entropy materials for catalysis: a new frontier. *Sci. Adv.* **7**, eabg1600 (2021).
9. Gao, S. et al. Synthesis of high-entropy alloy nanoparticles on supports by the fast moving bed pyrolysis. *Nat. Commun.* **11**, 2016 (2020).
10. Zhao, J. Z., Ahmed, T., Jiang, H.-X., He, J. & Sun, Q. Solidification of immiscible alloys: a review. *Acta Metall. Sin. (Engl. Lett.)* **30**, 1–28 (2017).
11. Miracle, D. B. & Senkov, O. N. A critical review of high entropy alloys and related concepts. *Acta Mater.* **122**, 448–511 (2017).
12. Yang, Y. et al. Aerosol synthesis of high entropy alloy nanoparticles. *Langmuir* **36**, 1985–1992 (2020).
13. Broge, N. L. N., Bondesgaard, M., Søndergaard-Pedersen, F., Roelsgaard, M. & Iversen, B. B. Autocatalytic formation of high entropy alloy nanoparticles. *Angew. Chem. Int. Ed.* **59**, 21920–21924 (2020).
14. Bondesgaard, M., Broge, N. L. N., Mamakhe, A., Bremholm, M. & Iversen, B. B. General solvothermal synthesis method for complete solubility range bimetallic and high entropy alloy nanocatalysts. *Adv. Funct. Mater.* **29**, 1905933 (2019).
15. Zhang, Y., Zhou, Y. J., Lin, J. P., Chen, G. L. & Liaw, P. K. Solid-solution phase formation rules for multi-component alloys. *Adv. Eng. Mater.* **10**, 534–538 (2008).
16. Murty, B. S., Yeh, J. W., Ranganathan, S. & Bhattacharjee, P. P. *High-Entropy Alloys* (Elsevier, 2019).
17. Si, J. et al. Chemical potential-modulated ultrahigh-phase-purity growth of ultrathin transition-metal boride single crystals. *J. Am. Chem. Soc.* **145**, 3994–4002 (2023).
18. Chen, Y. et al. Growth of 2D GaN single crystals on liquid metals. *J. Am. Chem. Soc.* **140**, 16392–16395 (2018).
19. Markwicka, E. J., Bartlett, M. D., Huang, X. & Majidi, C. An autonomously electrically self-healing liquid metal-elastomer composite for robust soft-matter robotics and electronics. *Nat. Mater.* **17**, 618–624 (2018).
20. Zavabeti, A. et al. A liquid metal reaction environment for the room-temperature synthesis of atomically thin metal oxides. *Science* **358**, 332–335 (2017).
21. Wang, W., Zhu, X. & Fu, L. Touch ablation of lithium dendrites via liquid metal for high-rate and long-lived batteries. *CCS Chem.* **2**, 686–695 (2020).
22. Esrafilzadeh, D. et al. Room temperature CO₂ reduction to solid carbon species on liquid metals featuring atomically thin ceria interfaces. *Nat. Commun.* **10**, 865 (2019).
23. Tang, J., Zhao, X., Li, J. & Liu, J. Thin, porous, and conductive networks of metal nanoparticles through electrochemical welding on a liquid metal template. *Adv. Mater. Interfaces* **5**, 1800406 (2018).
24. Takeuchi, A. & Inoue, A. Classification of bulk metallic glasses by atomic size difference, heat of mixing and period of constituent elements and its application to characterization of the main alloying element. *Mater. Trans.* **46**, 2817–2829 (2005).
25. Yao, Y. et al. Computationally aided, entropy-driven synthesis of highly efficient and durable multi-elemental alloy catalysts. *Sci. Adv.* **6**, eaaz0510 (2020).
26. Chang, X., Zeng, M. & Fu, L. Phase engineering of high-entropy alloys. *Adv. Mater.* **32**, 1907226 (2020).
27. Niu, H., Bonati, L., Piaggi, P. & Parrinello, M. Ab initio phase diagram and nucleation of gallium. *Nat. Commun.* **11**, 2654 (2020).
28. Zhao, L., Zong, H., Ding, X. & Lookman, T. Anomalous dislocation core structure in shock compressed bcc high-entropy alloys. *Acta Mater.* **209**, 116801 (2021).

Publisher's note Springer Nature remains neutral with regard to jurisdictional claims in published maps and institutional affiliations.

Springer Nature or its licensor (e.g. a society or other partner) holds exclusive rights to this article under a publishing agreement with the author(s) or other rightsholder(s); author self-archiving of the accepted manuscript version of this article is solely governed by the terms of such publishing agreement and applicable law.

© The Author(s), under exclusive licence to Springer Nature Limited 2023

Methods

Preparation of HEA-NPs

A certain amount of Ga was added into the solvent of 1-dodecanethiol and isopropanol and treated by sonication²⁹. The ultrasonication process is under 500-W power for 120 min. The mass volume ratio of Ga:1-dodecanethiol:isopropanol is 100:0.65:10. Under the ultrasonic cavitation and oscillating shear force, the Ga NPs were produced. Then, the mixture was centrifuged and washed with acetone to remove the solvent. Finally, the Ga NPs could be obtained after evaporating acetone at 343 K for a while. Considering that gallium could be oxidized under environmental conditions, the formed gallium oxide could play an important role as the protecting agent during the formation of Ga NPs²⁹. Additionally, the oxide layer would undergo thermo-mechanical fracture leakage upon heating owing to the thermal expansion mismatch between the liquid Ga and gallium oxide, resulting in the oxide coating fracture and ensuring the fluidity of Ga^{30,31}. Moreover, the low melting point of liquid metals originating from the anisotropic structure³² ensures the liquid environment for elemental mixing in the alloying process.

Before the synthesis of HEA-NPs, the precursors were prepared by mixing liquid metals (Ga, In and Sn) with various metal salts. The conversion from precursors to HEA-NPs was conducted in a horizontal tube furnace under the 50-sccm Ar and 300-sccm H₂ atmosphere. The furnace was heated up to 923 K within 30 min. After remaining for 6 h at 923 K, the furnace was naturally cooled down to room temperature. As a result, the HEA-NPs were obtained. Moreover, the HEA-NP loading on the silicon substrate and carbon black could also be prepared (Supplementary Fig. 34).

Material characterizations

Scanning electron microscopy (SEM) images were obtained from a ZEISS Merlin Compact SEM with EDS spectra collected by X-MaxN Oxford EDS. The XRD measurements were performed on a Rigaku Miniflex600 diffractometer equipped with Cu-K α radiation over the range of $2\theta = 10^\circ$ to approximately 80° . Additionally, the XRD data for Rietveld refinement were collected on a Rigaku SmartLabSE with Cu-K α radiation over the range of $2\theta = 10^\circ$ to approximately 120° . The specific compositions of HEA-NPs were determined with inductively coupled plasma–atomic emission spectrometry carried out on an IRIS Intrepid II XSP. The sample was predigested in a mixed solution of HCl and HNO₃.

For in situ SRXRD measurements, in situ XRD patterns were obtained at the BL02U2 Surface Diffraction Beamline of the Shanghai Synchrotron Radiation Facility with a wavelength of 1.2398 Å. The precursor composed of liquid metal and metal salts was placed onto the silicon substrate and put into the reaction chamber. A homemade in situ reaction chamber was established to allow for the heating, input and output of gas and water, where the circulation of water was utilized to protect the heating setup (Supplementary Fig. 31a). The grazing angle of the X-rays was set as 2° . The XRD pattern was recorded every 100 s in the heating and holding processes, while continuous sampling was performed in the cooling process. The integration time during the above three processes was 20 s.

Transmission electron microscopy characterization

Specimen preparation. For elemental analysis and atomic-scale HAADF-STEM imaging, the prepared HEA-NPs were dispersed in ethanol via the ultrasonic process. Then, the dispersion solution was drop casted onto the copper grid. For the in situ transmission electron microscopy experiment, a similar ultrasonic dispersion method was introduced to prepare precursor dispersion, and the dispersion was drop casted onto the plasma-cleaned Mo grid. The plasma pretreatment can effectively reduce the carbon deposition under electron irradiation in the in situ transmission electron microscopy observation. Before inserting the transmission electron microscopy holder

into an electron microscope, all the samples were cleaned under Ar/H₂ (25/5-sccm) atmosphere for 10 s.

In situ heating experiment of the precursor. To simulate the reaction process of the precursor in the tube furnace, an Mo grid with the precursor was loaded in a single-tilt heating holder (Gatan, Inc.). A ThermoFisher (previously FEI Titan ETEM G2 Cs-corrected ETEM) microscope was used to record the conversion process from the precursor to crystalline HEA-NPs under an H₂ atmosphere (20 mbar). Low accelerating voltage (80 kV) and an electron beam current density of 10–50 e⁻ Å⁻² s⁻¹ were applied to avoid the effect of the electron beam during the reaction process. The electron beam was blanked when the temperature ramped up. Supplementary Videos 1 and 2 were recorded at a frame rate of 30 frames s⁻¹. The HRTEM image and videos were acquired under an exposure time of 0.5 s by using a Ceta camera.

Ex situ experiments. For ex situ experiments, a double Cs-corrected (FEI Titan Themis G2) microscope (300 kV) equipped with EDS was used for elemental analysis and ex situ atomic-scale HAADF-STEM images operating at 300 kV. An FEI Super-X Quad windowless EDS detector based on silicon drift technology with a solid angle of 0.7 sr allowed for elemental mapping with a high signal-to-noise ratio. The images were acquired in HAADF-STEM mode with a convergence angle and a collection angle of 25 and 35–200 mrad, respectively. For elemental distribution of HEA-NPs, a Talos F200 equipped with a Super-X Quad windowless EDS detector was used to identify the species and distribution of elements in HEA-NPs. STEM imaging and EDS mapping were also acquired on a JEOL JEM-ARM200F microscope operated at 200 kV with a Schottky cold-field emission gun.

Computational methods of δ and ΔH_{mix}

The atom radii difference factor (δ) can be described as

$$\delta = \sqrt{\sum_{i=1}^N c_i \left(1 - \frac{r_i}{r}\right)^2} \quad (3)$$

where r is the average atomic radius in an alloy system, r_i is the atomic radius of the i th component, c_i is the percentage of atoms of the i th element and N is the total number of constituent elements in the HEAs.

The mixing enthalpy (ΔH_{mix}) can be quantified as

$$\Delta H_{\text{mix}} = \sum_{i=1, i \neq j}^n \Omega_{ij} c_i c_j \quad (4)$$

$$\Omega_{ij} = 4\Delta H_{AB}^{\text{mix}} \quad (5)$$

where c_i or c_j is the atomic percentage of the i th or j th component, respectively, and n is the number of components in the alloy system. $\Delta H_{AB}^{\text{mix}}$ represents the mixing enthalpy of binary AB alloys.

Molecular dynamics

The training dataset of the deep learning potential generating was obtained by ab initio molecular dynamics based on density functional theory calculations. The ab initio molecular dynamics calculation was carried out at 300 and 1,000 K in the canonical ensemble. Periodic boundary conditions and the Nosé–Hoover thermostat were employed to simulate the isothermal molecular dynamics of a 128-atom supercell for 10 ps.

The training of the interatomic potential for molecular dynamics simulations used a deep learning neural network architecture with three layers each having 250 nodes as implemented in the Deep Potential Smooth Edition package³³. The descriptors were constructed from all atomic configurations' information (both angular and radial), and the sizes of the embedding net are 25, 50 and 100 from left to right. The cutoff distance of 6 Å was set to represent the local internal structure

around any atom in our training dataset. During the training process, we used the sum of mean square deviations in energy, force and virial as the loss function and minimized it. The accuracy of the model is presented in Supplementary Table 10, and correlation plots for the testing and training data for the force predicted by the deep learning neural network related to that computed from density functional theory are shown in Supplementary Fig. 32.

To investigate the cooling process of GaMnFeNiCu, the molecular dynamics simulations were implemented by the Large-Scale Atomic/Molecular Massively Parallel Simulator³⁴. All of our cooling studies were performed from 1,000 to 300 K, and the system consisted of 16,000 atoms in a $57.8 \times 57.8 \times 57.8\text{-}\text{\AA}$ box with periodic boundary conditions in all three dimensions. The cooling molecular dynamics simulation of 10 ns was carried out by deep learning potential.

Data availability

Source data are provided with this paper.

Code availability

The code is publicly available in the GitHub repository at <https://github.com/XuhaoWan/HEA-LM>.

29. Yamaguchi, A., Mashima, Y. & Iyoda, T. Reversible size control of liquid-metal nanoparticles under ultrasonication. *Angew. Chem. Int. Ed.* **54**, 12809–12813 (2015).
30. Cutinho, J. et al. Autonomous thermal-oxidative composition inversion and texture tuning of liquid metal surfaces. *ACS Nano* **12**, 4744–4753 (2018).
31. Martin, A., Kiarie, W., Chang, B. & Thuo, M. Chameleon metals: autonomous nano-texturing and composition inversion on liquid metals surfaces. *Angew. Chem. Int. Ed.* **59**, 352–357 (2020).
32. Daeneke, T. et al. Liquid metals: fundamentals and applications in chemistry. *Chem. Soc. Rev.* **47**, 4073–4111 (2018).

33. Zhang, L. et al. End-to-end symmetry preserving inter-atomic potential energy model for finite and extended systems. In *Proc. 32nd International Conference on Neural Information Processing Systems* (ed. Bengio, S. et al.) 4441–4451 (Curran Associates, 2018).
34. Plimpton, S. Fast parallel algorithms for short-range molecular dynamics. *J. Comput. Phys.* **117**, 1–19 (1995).

Acknowledgements We thank the Core Facility of Wuhan University for providing the inductively coupled plasma-atomic emission spectrometry tests. We also thank the Core Research Facilities of the College of Chemistry and Molecular Sciences at Wuhan University for the SEM characterization, the Shanghai Synchrotron Radiation Facility for the in situ X-ray diffraction and the Center for Electron Microscopy at Wuhan University for their substantial support of transmission electron microscopy characterization. The research was supported by the National Natural Science Foundation of China (Grants 22025303, 21905210 and 11974156); the National Youth Talent Support Program; the Inner Mongolia Natural Science Foundation (Grant 2019MS02006); the Program for Young Talents of Science and Technology in Universities of Inner Mongolia Autonomous Region (Grant NJYT-20-B10); the Guangdong Innovative and Entrepreneurial Research Team Program (Grant 2019ZT08C044); the Shenzhen Science and Technology Program (Grants KQTD20190929173815000 and 20200925161102001); and the Science, Technology and Innovation Commission of Shenzhen Municipality (Grant ZDSYS20190902092905285). We also received assistance from the SUSTech Core Research Facilities, especially technical support from Pico Centre, which receives support from the Presidential Fund and the Development and Reform Commission of Shenzhen Municipality.

Author contributions L.F. conceived the research concept. L.F. and M.Q.Z. supervised the research. G.H.C., J. Liang and K.N.Y. carried out the main experiments. J. Lin, Z.G., G.W. and Y.F. performed transmission electron microscopy characterizations. Y.G., X.W. and Z. Li contributed to theoretical calculation. Y.B. conducted the Rietveld refinement. H.W., Y.Z., J. Liu, G.H. and Z.X. contributed to sample preparation. L.F., M.Z., G.C., J. Liang and K.Y. cowrote the manuscript. All the authors contributed to data analysis and scientific discussion.

Competing interests The authors declare no competing interests.

Additional information

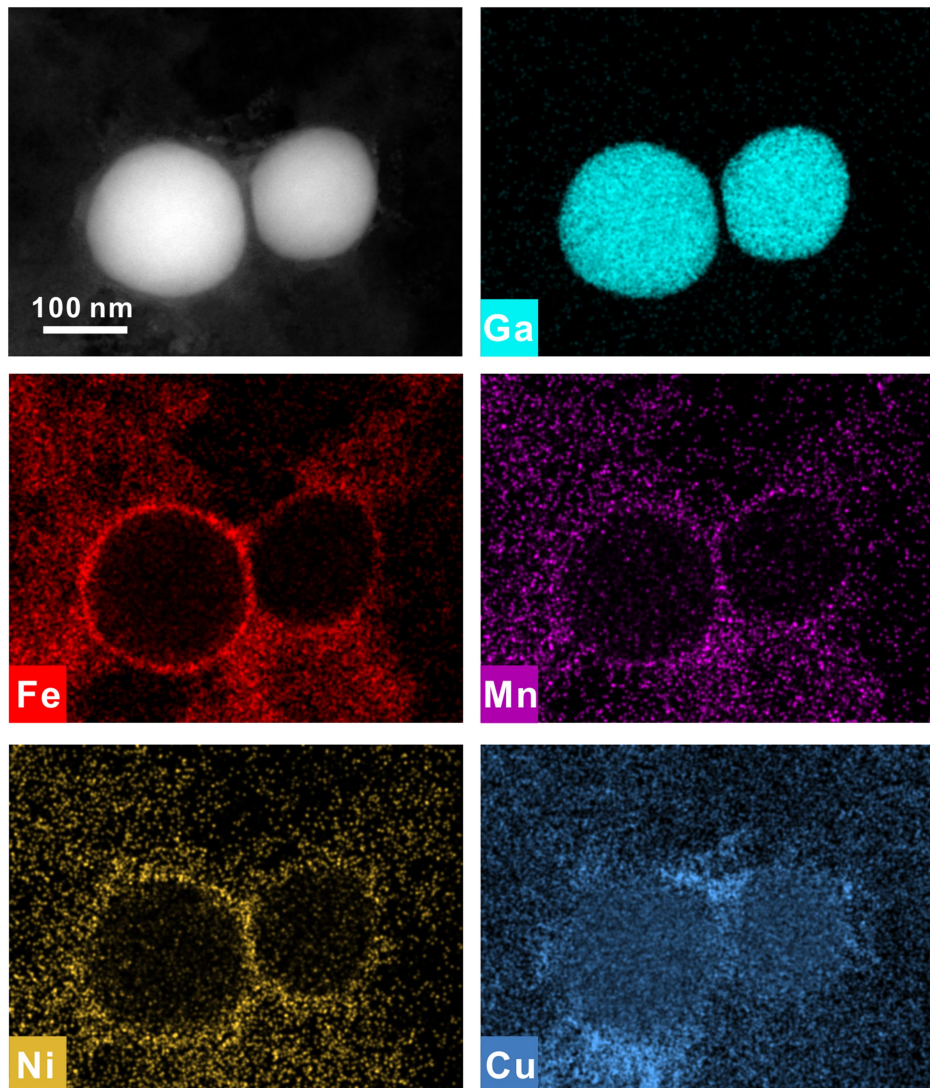
Supplementary information The online version contains supplementary material available at <https://doi.org/10.1038/s41586-023-06082-9>.

Correspondence and requests for materials should be addressed to Yuzheng Guo, Mengqi Zeng, Junhao Lin or Lei Fu.

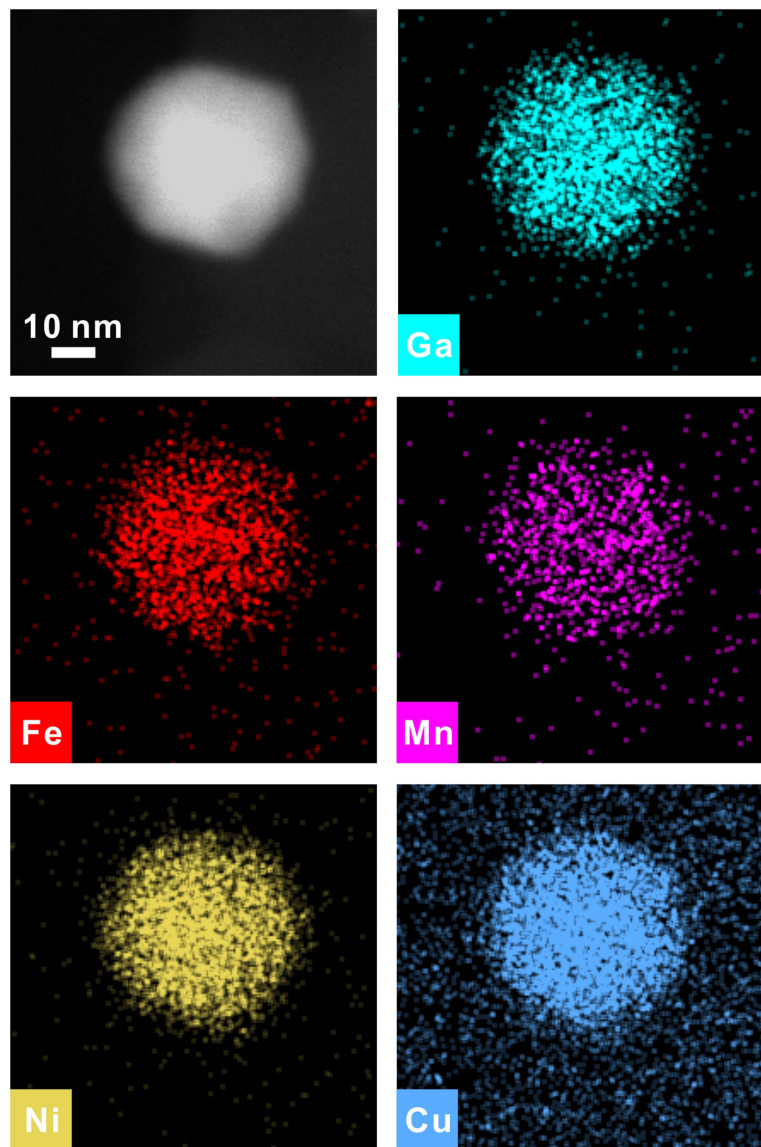
Peer review information *Nature* thanks Liangbing Hu, Yong Yang and the other, anonymous, reviewer(s) for their contribution to the peer review of this work.

Reprints and permissions information is available at <http://www.nature.com/reprints>.

Article

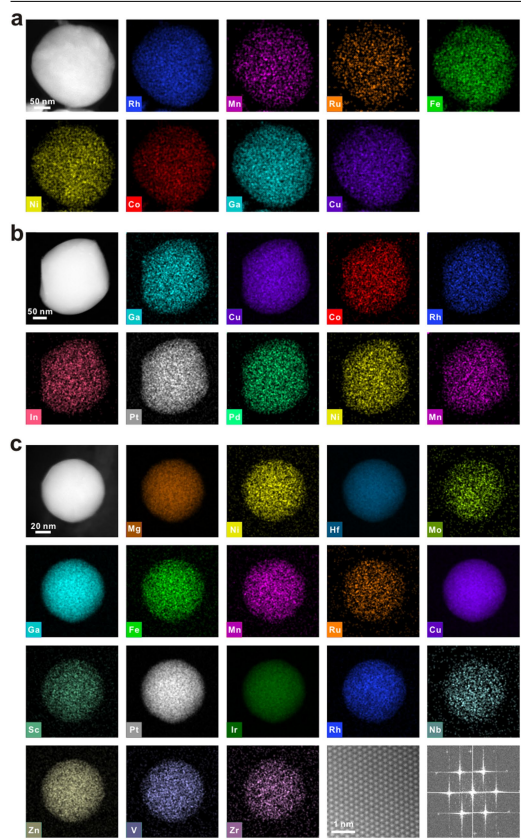


Extended Data Fig. 1 | The TEM-EDS mapping of the precursor with adjacent Ga NPs. The metal salts are uniformly distributed around Ga NPs. There is a clear boundary between metal salts and Ga NPs. Moreover, the contrast of Cu elemental mapping could be affected by the copper grid.

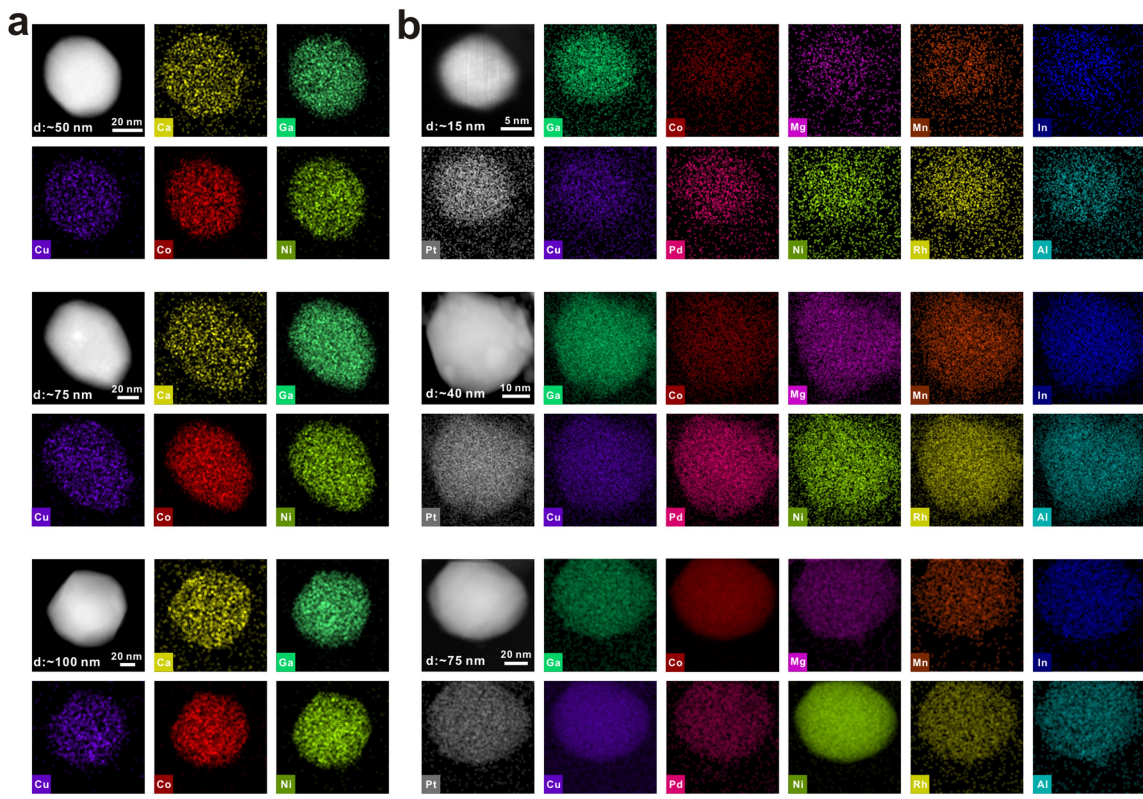


Extended Data Fig. 2 | The TEM EDS mapping of GaFeMnNiCu product via the reaction process in the furnace tube, exhibiting a uniform elemental distribution.

Article



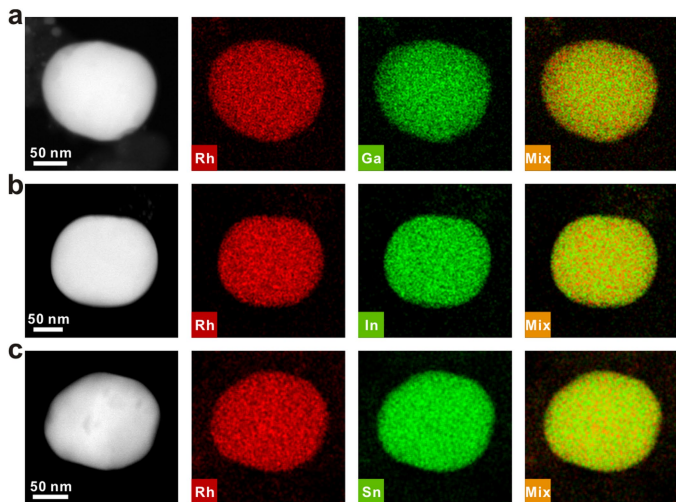
**Extended Data Fig. 3 | STEM elemental maps of octenary
(GaMnNiCuRuRhFeCo), novenary (GaCuPdNiMnInRhPtCo), and 17
(GaFeNiCuZnScVMnMgZrPtRhRuIrHfMoNb) HEA-NPs, respectively.
All HEA-NPs exhibit uniform element distribution.**



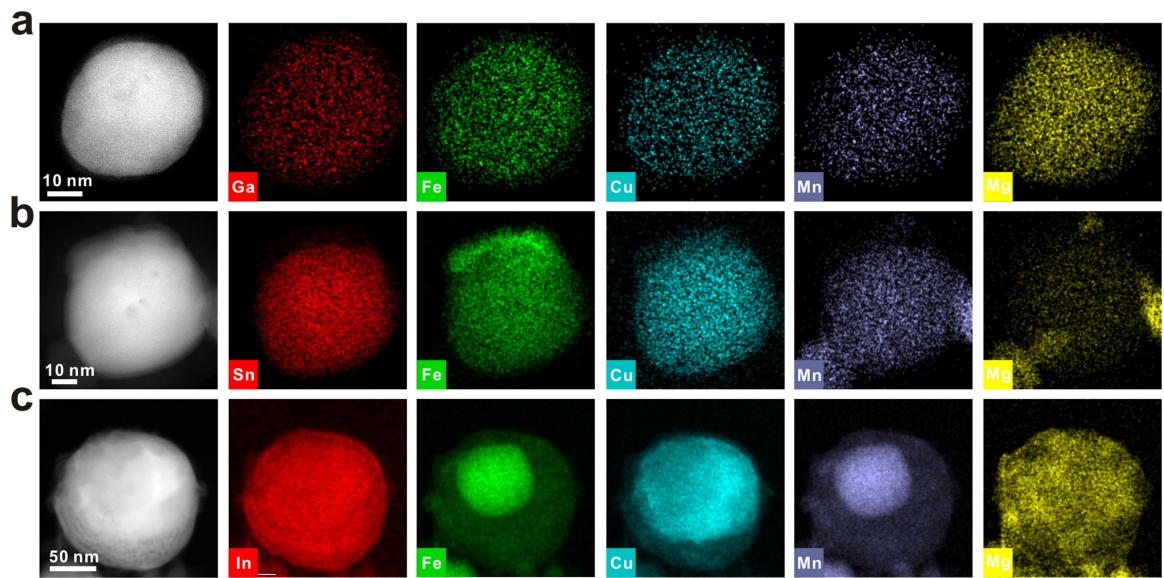
Extended Data Fig. 4 | Elemental characterization of HEA-NPs with different diameters. **a**, STEM elemental maps of the HEA-NPs (GaCaCoNiCu) with different sizes of about 50 nm, 75 nm, and 100 nm, respectively. **b**, STEM

elemental maps of the HEA-NPs (GaCuPdNiMnAlInRhPtCoMg) with different sizes of about 15 nm, 40 nm, and 75 nm, respectively. All HEA-NPs exhibited uniform elemental distribution.

Article

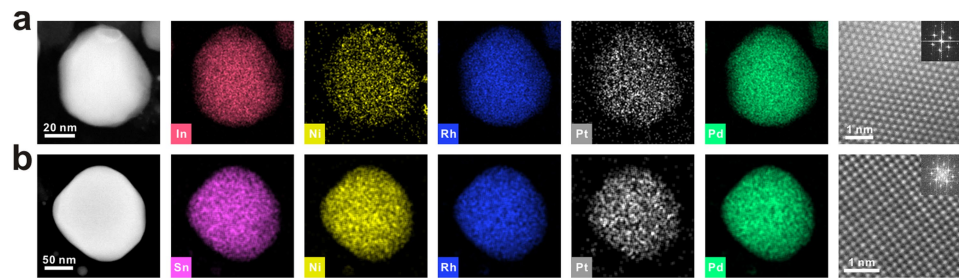


Extended Data Fig. 5 | The STEM-EDS elemental maps of GaRh, InRh, and SnRh, respectively, exhibiting a uniform elemental distribution.

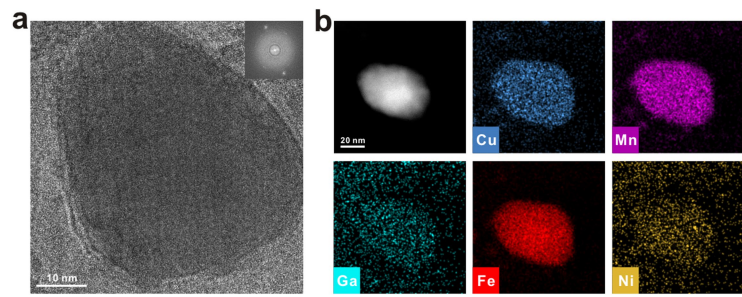


Extended Data Fig. 6 | The STEM-EDS elemental maps of GaFeMnMgCu, SnFeMnMgCu, and InFeMnMgCu HEA-NPs, respectively, exhibiting different elemental mixing states.

Article



Extended Data Fig. 7 | The elemental and structural characterization of InNiRhPtPd and SnNiRhPtPd HEA-NPs, respectively, indicating the uniform elemental distribution for both alloy systems.



Extended Data Fig. 8 | TEM characterization of an individual GaFeMnNiCu nanoparticle after in situ reaction. **a**, TEM image and FFT analysis (inset) of the nanoparticle, showing the occurrence of crystallization. **b**, The EDS

mapping of the nanoparticle. The uniform elemental distribution indicates the elements can be alloyed into a nanoparticle by the in situ reaction process.